A filtering method to correct time-lapse 3D ERT data and improve imaging of natural aquifer dynamics

Ilaria Coscia[1], Niklas Linde[2], Stewart Greenhalgh[1,3], Thomas Günther[4], Alan Green[1]

[1]Institute of Geophysics, ETH Zurich, Sonnegstrasse 5, 8092 Zurich, Switzerland;

[2]Institute of Geophysics, University of Lausanne, Amphipôle – UNIL SORGE, 1015 Lausanne, Switzerland;

[3]Department of Physics, University of Adelaide, Adelaide, Australia;

[4]Leibniz Institute for Applied Geophysics, Hannover, Germany.

[*] Corresponding author: niklas.linde@unil.ch

ABSTRACT

We have developed a processing methodology that allows crosshole ERT (electrical resistivity tomography) monitoring data to be used to derive temporal fluctuations of groundwater electrical resistivity and thereby characterize the dynamics of groundwater in a gravel aquifer as it is infiltrated by river water. Temporal variations of the raw ERT apparent-resistivity data were mainly sensitive to the resistivity (salinity), temperature and height of the groundwater, with the relative contributions of these effects depending on the time and the electrode configuration. To resolve the changes in groundwater resistivity, we first expressed fluctuations of temperature-detrended apparent-resistivity data as linear superpositions of (i) time series of river-water-resistivity variations convolved with suitable filter functions and (ii) linear and quadratic representations of river-water-height variations multiplied by appropriate sensitivity factors; river-water height was determined to be a reliable proxy for groundwater height. Individual filter functions and sensitivity factors were obtained for each electrode configuration via deconvolution using a one month calibration period and then the predicted contributions related to changes in water height were removed prior to inversion of the temperature-detrended apparent-resistivity data. Applications of the filter functions and sensitivity factors accurately predicted the apparent-resistivity variations (the correlation coefficient was 0.98). Furthermore, the filtered ERT monitoring data and resultant time-lapse resistivity models correlated closely with independently measured groundwater electrical resistivity monitoring data and only weakly with the groundwater-height fluctuations. The inversion results based on the filtered ERT data also showed significantly less inversion artefacts than the raw data inversions. We observed resistivity increases of up to 10% and the arrival time peaks in the time-lapse resistivity models matched those in the groundwater resistivity monitoring data.

1. Introduction

Growing scientific and regulatory interest in interactions between surface water and groundwater has led to the increased use of geophysical methods for characterizing hyporheic processes and aquifer systems that are connected to the sea, lakes, and rivers. Geophysical methods are used to derive conceptual models of contact zones (e.g., river beds), define the interior structure of connected aquifers (e.g., Acworth and Dasey, 2003; Crook et al., 2008; Nguyen et al., 2009; Hatch et al., 2010; Doetsch et al., 2010b; Slater et al., 2010), and obtain information about surface water - groundwater interactions. The latter is achieved by analyzing geophysical time series or time-lapse inversion models following natural (e.g., Nyquist et al., 2008; de Franco et al., 2009; Fàlgas et al., 2009; Ogilvy et al., 2009; Slater et al., 2010) or artificial perturbations of the system, for example, in the form of saline tracers injected into a river (Ward et al., 2010).

There are numerous hydrological methods for studying river water - groundwater interactions (e.g., Kalbus et al., 2006; Cook et al., 2003). Many of them exploit natural fluctuations of state variables (e.g., temperature) or isotope concentrations. One well-established approach is to compare river and groundwater heights to determine if a river is losing or gaining water. Similar information is obtained at larger scales by analyzing differences in discharge between river cross sections (Harvey and Wagner, 2000). Temperature variations in a river and in adjacent groundwater can be used to identify recharge or discharge zones and to quantify water fluxes at the river - aquifer interface (Anderson, 2005); fibre-optic-distributed sensors now make it possible to obtain temperature data at very high spatial and temporal resolutions (e.g., Selker et al., 2006; Slater et al., 2010). As for temperature measurements, electrical resistivity time series of river water and groundwater can be used to infer traveltimes of water moving from rivers to groundwater observation boreholes (e.g., Cirpka et al., 2007; Vogt et al., 2010). However, using these techniques alone

makes it extremely difficult to delineate the evolution of three-dimensional (3D) groundwater flow patterns in the vicinity of rivers. Geophysical methods may provide key complementary 3D information.

Natural sources in the form of fluctuations of river water resistivity offer several advantages over artificial ones when studying surface water and groundwater dynamics using geophysical techniques. The resultant data provide more integrated information because they are unaffected by local heterogeneities close to the injection points, the field experiments are less expensive, and permits are easier to obtain. Furthermore, using natural sources is the only viable option for obtaining meaningful geophysical responses when working in large rivers or catchments (Yeh et al., 2008).

A major complication of geophysical monitoring based on natural-source signals is that the effects of interest are often superimposed on other unwanted signals. As a consequence, geophysical monitoring can only provide spatial and temporal distributions of a time-varying property if the corresponding geophysical signal dominates or if it can be isolated from signals originating from other time-varying phenomena (Rein et al., 2004). Electrical resistivity tomography (ERT) monitoring data used in this study are not only affected by resistivity (salinity) variations in the pore water (i.e., the natural tracer of interest), but also by variations in groundwater temperature and height. ERT methodology is treated by Binley and Kemna (2005) and the relationships between electrical and hydrogeological properties and state variables are reviewed by Lesmes and Friedman (2005).

Different approaches for removing unwanted temporally-varying contributions from ERT data or inversion models have been proposed. For example, Olofsson and Lundmark (2009) performed long-term ERT monitoring to evaluate how de-icing salt affects the roadside subsurface. They evaluated temporal variations by comparing them with models obtained in areas with similar geological characteristics, but where no de-icing salt had been applied. This

approach can be problematic as a good reference site is often difficult to find. Hayley et al. (2007; 2009; 2010) sought to image variations in pore-water salinity. This task was complicated by variations in temperature and water content that also affected the ERT measurements. They evaluated two possible ways to remove the unwanted effects. The first approach was to apply post-inversion corrections to the inversion models and thereby convert them to reference temperature and saturation conditions (Hayley et al., 2007, 2009). This method required specific petrophysical relationships between the unwanted variables (temperature and water saturation) and the electrical properties, together with measurements of these variables at discrete locations. A better performing approach involved applying pre-inversion corrections to the data based on differences between simulated data from unreferenced and referenced inversion models obtained from the first approach (Hayley et al., 2010).

Only a few geophysical studies have exploited natural variations to characterize river - groundwater interactions. Nyquist et al. (2008) investigated such interactions by performing an electrical resistivity survey within a river; two ERT profiles collected at different river stages were compared and the differences in the resistivity models were interpreted in terms of groundwater discharge patterns. Slater et al. (2010) provided constraints to a conceptual model describing flow pathways of contaminated groundwater leaking into a river by combining continuous waterborne electrical imaging with high-resolution temperature monitoring; static inversion of the ERT and time-domain induced polarization data provided a general hydrogeologic zonation, whereas the temperature variations indicated the locations of river and groundwater exchange.

We have acquired more than one year of 3D crosshole ERT monitoring data close to the Thur River in Switzerland (Fig. 1a). The electrical stratigraphy of the aquifer is known from an earlier study (Coscia et al., 2011). Here, we investigate the extent to which infiltrating river

water can be used as a natural tracer for imaging aquifer dynamics. Electrical resistivity fluctuations in the river water and groundwater have previously been used at this site to infer traveltime distributions (Cirpka et al., 2007). In contrast, we focus on ERT apparent-resistivity data that we eventually want to use to image 3D groundwater flow patterns.

To achieve this ultimate goal, we develop here a temporal filtering methodology to remove the effects of seasonal variations in temperature and relatively rapid groundwater-height fluctuations from our apparent resistivity time series before performing time-lapse inversions. Minimizing these effects is crucial for obtaining time-lapse images that are primarily related to changes in groundwater resistivity. Our method involves expressing the temperature-detrended ERT data variations as a function of two variables: the filtered variations of river-water resistivity and a quadratic expression of the instantaneous river height. A one-month period of data was used to estimate, for each electrode configuration, the coefficients of the quadratic expression by deconvolving apparent resistivity time series with river-water resistivity and river height time-series.

After introducing the study site and the various data sets, we outline how we correct the river-water and groundwater resistivities and ERT apparent resistivities for seasonal temperature variations. We then concentrate on our method for minimizing the effects of changing groundwater height on the temperature-detrended apparent resistivities before describing the time-lapse inversions and initial comparisons with groundwater monitoring data.

2. Study site, experiment, and data

2.1 Study site and experimental description

Our study site is located at Widen in the Thur catchment of northeastern Switzerland (Fig. 1a). At this location, the Thur River infiltrates an adjacent aquifer consisting of silty

gravel (Cirpka et al., 2007; Diem et al., 2010). The aquifer is approximately 7 m thick. It is embedded between an overlying 3-m-thick layer of loam and an underlying aquitard of fine lacustrine clay (Fig. 1c).

Details on the site, instrumentation, installation, and our recording strategy are given by Coscia et al. (2011). Only a summary of this information is provided here. The experimental set-up includes eighteen ~11-m-deep boreholes evenly spaced at 3.5 m intervals (Fig. 1b and c). They each contain a slotted plastic casing and a geoelectric cable with 10 electrodes spaced 0.7 m apart along the length of the aquifer section. The cables are centred in the middle of the boreholes with the borehole fluid providing the electrical contact between the electrodes and the aquifer. An ERT measuring device, a computer that controls the measurements, and a wireless system that allows the computer and recorded data to be accessed remotely are installed in a flood-proof hut. A number of boreholes are also equipped with sensors and loggers at three different depths (~ 4.6 m, ~ 6.6 m, and ~ 8.6 m) to measure groundwater height, temperature, pressure, and resistivity every 15 minutes. Sensors and a logger are also installed at a river station ~50 m downstream of the study site.

Under normal river conditions (i.e., river discharge $\sim 47\ m^3/s$; data from www.hydrodaten.admin.ch), the upper ~ 1 m of the gravel aquifer is unsaturated. Under very high discharge conditions (i.e., $> 500\ m^3/s$), the aquifer is fully saturated and it behaves as a confined system. The geometric mean of the aquifer's hydraulic conductivity estimated from borehole slug tests is 4.2×10^{-3} m/s (Diem et al., 2010).

Using an innovative circulating 3D electrode measuring scheme (Coscia et al., 2011), one apparent-resistivity measurement was made for each of 15,500 different electrode configurations every ~7 h. The internal structure of the aquifer was studied in detail through static 3D ERT inversions of one of these 7-h data sets collected during stable hydrological conditions (Coscia et al., 2011). The aquifer was characterized by a central 2-m-thick more

resistive middle layer (~ 300 Ω.m) that corresponded to a zone of lower porosity (~ 20 %). In the lower part of the gravel aquifer and away from the river, the resistivity decreased, implying an increase of fine sediments at these locations. Further information on the aquifer structure, deduced not only from ERT, but also from crosshole ground-penetrating radar and seismic investigations, is provided by Doetsch et al. (2010a; 2010b), Klotzsche et al. (2010), and Coscia et al. (2011).

2.2 ERT apparent-resistivity and hydrological time series

ERT apparent-resistivity data were acquired from March 2009 until December 2010. The ERT data set has several gaps, mainly because of instrumental problems. Nevertheless, more than one year of apparent-resistivity data are available, with several periods of continuous recordings exceeding one month.

The apparent-resistivity data are intended to image natural variations in the aquifer related to the changing characteristics of the infiltrating river water at different temporal scales: seasonal, diurnal, and individual rainfall-runoff events (i.e., about a week). Such data could be used to investigate river-water infiltration rates, mixing processes, residence times, 3D permeability structure of the aquifer, and flow-path geometry. In this study, we focus on a new method to distinguish fluctuations in apparent resistivity caused by variations in groundwater resistivity ρ^{gw} from those due to variations in groundwater height h^{gw} at the time-scale of rainfall-runoff events (see Table 1 for definitions of the variables used in this contribution). We begin by describing the hydrological variables that are expected to have an impact on the raw apparent resistivities ρ_a^{raw}.

The bulk electrical resistivity of an aquifer is largely determined by pore-water resistivity ρ^{gw}, which is controlled by the concentration of dissolved solids (e.g., salts) in the water, as well as water saturation, porosity, and clay content (Lesmes and Friedman, 2005). Bulk

resistivity decreases with increasing concentrations of dissolved solids and increasing water saturation, whereas the porosity term includes not only the volume fraction of pore space in the rock but also the shape and connectivity of the pores. Temperature also has an influence on bulk electrical resistivity, with resistivity tending to decrease as temperature increases.

Heavy precipitation in the Thur catchment results in large volumes of rainwater rapidly entering the river system, either directly or via short travel paths on the surface or through the ground. This water tends to have a low salinity and, as a consequence, have a higher resistivity than river water under low- to moderate flow conditions (Cirpka et al., 2007). Accordingly, significant periods of precipitation result in strong and rather sharp increases in river-water electrical resistivity ρ^{rw} (Fig. 2a). Because the resistive river water constantly infiltrates the adjacent aquifer at the study site, it can be used as a natural tracer for estimating groundwater traveltimes from the infiltration point to observation or water-supply boreholes at distances up to hundreds of meters from the river (Cirpka et al., 2007; Vogt et al., 2010). Fig. 2a shows that variations in groundwater resistivity ρ^{gw} are markedly damped (e.g., by a factor of ~6) and delayed (4-7 days, depending on the location) relative to ρ^{rw} for the 1-month period that we use for calibration.

Following precipitation in the upper part of the catchment, the channelized Thur River is subject to rapid variations in discharge and river height along its entire course. As examples, intense precipitation caused the discharge to increase from 25 to 750 m^3/s during the most extreme event of Summer 2009 and from 42 to 232 m^3/s during the first significant rainfall-runoff event during the calibration period. Fig. 2b demonstrates that the latter event resulted in fast and practically coincident variations of river-water height h^{rw} and groundwater height h^{gw}, but that the maximum variations of h^{gw} were roughly half those of h^{rw}. Variations of h^{gw} strongly affect ρ_a^{raw}, because h^{gw} determines the fractional volume of the aquifer that is saturated. As a consequence, variations in h^{gw} lead to practically coincident variations in ρ_a^{raw}

that can mask the responses related to changes in the groundwater resistivity ρ^{gw} caused by the resistive river water ρ^{rw} infiltrating the aquifer.

Every hydrological event also creates variations of river-water temperature T^{rw} (solid line in Fig. 2c). In contrast, variations in groundwater temperature T^{gw} (dashed line in Fig. 2c) appear to be dominated by seasonal trends (best observed in the one year of temperature data displayed in Fig. 3a) and only weakly affected by river-water temperature fluctuations associated with changes in river-water discharge. The maximum variation of groundwater temperature T^{gw} during the one-month calibration period is ~4 °C (Table 2), corresponding to an ~8% variation of ρ^{gw} (Lesmes and Friedman, 2005).

It thus appears that variations of ρ^{gw} and h^{gw} at the scale of single hydrological events are the most important causes of natural fluctuations of ρ_a^{raw}. Nevertheless, it is necessary to account for the effects of seasonal temperature fluctuations before attempting to separate the ρ^{gw} and h^{gw} contributions because they would otherwise have an effect on the final resistivity model time series. Our complete processing scheme is summarized in Fig. 4.

3. Preprocessing

Before considering the effects of changing river-water and groundwater heights and resistivities on ρ_a^{raw}, it was necessary to apply some preprocessing to the different data sets (Fig. 4 and Table 2). We first removed variations in the measured time series at periods shorter than the 7-h period used to acquire a single complete ERT apparent-resistivity data set. To achieve this, the $\boldsymbol{\rho}^{rw}$, $\boldsymbol{\rho}^{gw}$, $\mathbf{h}^{rw}$, and $\mathbf{h}^{gw}$ time series (data series and filter functions are marked bold in the following) were passed through a fourth-order low-pass Butterworth filter with a cut-off frequency corresponding to a period of 7 h.

Long-term variations in $\boldsymbol{\rho}^{rw}$ and $\boldsymbol{\rho}^{gw}$ were mainly due to snow melting in the upper part of the catchment and effects of temperature variations in $\mathbf{T}^{rw}$ and $\mathbf{T}^{gw}$. The original $\boldsymbol{\rho}^{rw}$ values

(Department of the Environment, Canton Thurgau) and $\boldsymbol{\rho}^{gw}$ values had been automatically corrected to a constant temperature of 25 ^{o}C according to procedures described in ISO7888 (1985). Clearly, this temperature was too high for our study (Fig. 3a and Table 2). Therefore, each estimate of ρ^{rw} and ρ^{gw} in the respective time series was adjusted from their values at 25 ^{o}C to the yearly median temperatures at our site (T^{rw} = 9.8 °C and T^{gw} = 10.7 °C) using correction factors provided in ISO7888 (1985).

The effects of seasonal variations of $\mathbf{T}^{gw}$ (Fig. 3a) on the apparent resistivities were minimized by multiplying the $\boldsymbol{\rho}_a^{raw}$ data for each ERT electrode configuration by a diagonal matrix with diagonal entries $(1 + k\Delta\mathbf{T}^{gw})$, where $\Delta\mathbf{T}^{gw}$ were values relative to the yearly median of $\mathbf{T}^{gw}$ measured at one of the groundwater loggers (P3, approximately 10 m from the river at ~ 6.6 m depth). For each ERT electrode configuration, we let k vary to determine the optimum k value that minimized the correlation between the temperature-detrended apparent resistivities $\boldsymbol{\rho}_a$ and $\Delta\mathbf{T}^{gw}$. Typical values of k were in the 0.01 - 0.03 $(C^{\circ})^{-1}$ range, with a mean of 0.017 $(C^{\circ})^{-1.}$ These values were close to coefficients used to relate apparent resistivity to temperature in several other studies (e.g., Rein et al., 2004; Hayley et al., 2010).

Configuration-specific k values were required to account for the variation in amplitudes of temperature changes in the unsaturated gravel, gravel aquifer and aquitard and the volume-averaged nature of apparent resistivity variations. Essentially, the sensitivity patterns that influenced the apparent resistivities were different for each configuration. Note also that this correction approach was based on the assumption that phase differences of $\Delta\mathbf{T}^{gw}$ perturbations within the aquifer were negligible when considering seasonal variations. The results of applying our temperature-correction scheme to a $\boldsymbol{\rho}_a^{raw}$ time series recorded by a typical ERT electrode configuration are shown in Fig. 3b.

4. Accounting for groundwater-height variations

Changes in h^{gw} cause changes in apparent-resistivity ρ_a that depend on the particular electrode configuration used. Increases in h^{gw} mostly, but not always, result in decreases in ρ_a, because part of the more resistive unsaturated zone of the aquifer is replaced by a less resistive saturated zone. There are several different approaches for minimizing the effect of changes in h^{gw} on ρ_a.

One approach would be to include h^{gw} as a known temporally varying interface within the time-lapse inversion process. Unfortunately, such an approach would require remeshing the forward and inversion grids at each time step, which would make it difficult to distinguish numerical errors from small changes in ρ^{gw}. A strong motivation for adopting time-lapse inversion procedures is that modelling errors largely cancel. Because modelling errors are sensitive to the forward mesh, this advantage would be lost if frequent remeshing was required.

A second approach would be to numerically model the effects of h^{gw} variations and then remove them from the ρ_a data sets. The main problem with this approach is that detailed information on the electrical resistivity structure of both the saturated and unsaturated parts of the aquifer would be needed. Fig. 5 displays simulated apparent resistivities as functions of changes in h^{gw} for two electrode configurations used in this study, assuming an idealized two-layered model in which the electrical resistivities of the saturated and unsaturated zones are 250 and 600 Ω.m, respectively. Note, that the curves are weakly non-linear (e.g., parabolic) and that ρ_a can either increase or decrease with increasing h^{gw}, depending on the electrode configuration and placement. Results from other models (not shown) indicate that the slope of the relationship (i.e., the sensitivity function) is strongly dependent on the typically poorly known electrical resistivity of the unsaturated zone.

The third approach is to use measured time series of the relevant variables to estimate the influence of h^{gw} on ρ_a. We adopt this approach and develop and test the necessary methodology.

4.1. Hypotheses and formalism of the filtering method

In the following, we relate variations in temperature-detrended apparent resistivity $\Delta\boldsymbol{\rho}_a$ to variations in temperature-detrended river-water resistivity $\Delta\boldsymbol{\rho}^{rw}$ and river-water height $\Delta\mathbf{h}^{rw}$ (the Δ values are deviations from the yearly median estimates; see Tables 1 and 2). River-water resistivity and height are recorded at the same location ~50 m downstream of our study site. Fig. 2b demonstrates that $\Delta\mathbf{h}^{rw}$ is a dependable proxy for $\Delta\mathbf{h}^{gw}$; there are no appreciable phase differences between the two signals at our study site (a few seconds compared to the sampling interval of 7 h), only amplitude differences, with the river signal being the larger. Note that using $\Delta\mathbf{h}^{gw}$ directly would be a better choice if sources other than the river affected $\Delta\mathbf{h}^{gw}$ or if $\Delta\mathbf{h}^{gw}$ is significantly delayed with respect to $\Delta\mathbf{h}^{rw}$.

Our method is based on the assumption that changes in apparent resistivity $\Delta\rho_a$ for a given electrode configuration and specified time can be viewed as the superposition of (i) the weighted (filtered) combination of present and past $\Delta\boldsymbol{\rho}^{rw}$ values, and (ii) the present $\Delta\mathbf{h}^{rw}$ and $(\Delta\mathbf{h}^{rw})^2$ values. The quadratic term in the water height is required to account for the slightly non-linear relationship between $\Delta\boldsymbol{\rho}_a$ and $\Delta\mathbf{h}^{gw}$ (see Fig. 5 and the corresponding section on modelling the $\mathbf{h}^{gw}$ effect). No such quadratic terms are needed for $\Delta\boldsymbol{\rho}^{rw}$, because the relationship between $\Delta\boldsymbol{\rho}_a$ and $\Delta\boldsymbol{\rho}^{gw}$ is close to linear as a consequence of the small relative changes in $\Delta\boldsymbol{\rho}^{gw}$ and the close to linear relationship between $\boldsymbol{\rho}^{gw}$ and bulk resistivity. Furthermore, Cirpka et al (2007) found a linear relationship between $\Delta\boldsymbol{\rho}^{rw}$ and $\Delta\boldsymbol{\rho}^{gw}$ using data from the river and borehole loggers. Accordingly, $\Delta\boldsymbol{\rho}_a$ for a given electrode configuration can be described by a convolution of the $\Delta\boldsymbol{\rho}^{rw}$ time series with smoothly varying causal

impulse response functions $\mathbf{f}^{\rho}$, where the superscript ρ refers to river-water resistivity variations, and the multiplication of present values of $\Delta\mathbf{h}^{rw}$ and $(\Delta\mathbf{h}^{rw})^2$ by sensitivity factors *a* and *b*.

We assume that variations in $\Delta\boldsymbol{\rho}^{gw}$ have a negligible influence on the $\Delta\mathbf{h}^{gw}$ effect, since variations in $\Delta\boldsymbol{\rho}^{gw}$ are on the order of 10%, whereas electrical resistivity variations in the vicinity of the fluctuating groundwater table are expected to exceed 100% due to the strong influence of water content.

The input function $\Delta\boldsymbol{\rho}^{rw}$ can be written as:

$$\Delta\boldsymbol{\rho}^{rw} = (...\Delta\rho^{rw}_{-3},\ \Delta\rho^{rw}_{-2},\ \Delta\rho^{rw}_{-1},\ \Delta\rho^{rw}_{0},\ \Delta\rho^{rw}_{1},\ \Delta\rho^{rw}_{2},\ \Delta\rho^{rw}_{-3},\ ...)^{\mathsf{T}}, \tag{1}$$

where superscript $\mathbf{T}$ denotes the transpose operator, zero subscript refers to when the first ρ_a value is measured, negative subscripts refer to earlier times, and positive subscripts to later times. The output apparent-resistivity time series is given by:

$$\Delta\boldsymbol{\rho}_a = (\Delta\rho_{a,0}, \Delta\rho_{a,1}, \Delta\rho_{a,2}, \Delta\rho_{a,3}, \Delta\rho_{a,4}, ...)^{\mathsf{T}}. \tag{2}$$

Because the filter $\mathbf{f}^{\rho}$ is causal, it only comprises entries for positive times. It can be written as:

$$\mathbf{f}^{\rho} = (f_0^{\rho}, f_1^{\rho}, f_2^{\rho}, f_3^{\rho} ..... f_M^{\rho})^{\mathsf{T}}, \tag{3}$$

where *M* is the filter length that needs to be chosen such that the whole transient phenomenon is represented. We can now write out $\Delta\rho_a$ for each electrode configuration in terms of the convolution $\mathbf{f}^{\rho} * \Delta\boldsymbol{\rho}^{rw}$ and the multiplications $a\Delta\mathbf{h}^{rw}$ and $b(\Delta\mathbf{h}^{rw})^2$ for a given time *j* as:

$$\Delta\rho_{a,j} \approx \sum_{k=0}^{N} f_k^{\rho}\Delta\rho^{rw}_{j-k} + a\Delta h_j^{rw} + b\left(\Delta h_j^{rw}\right)^2 \qquad j = 0,1,2,3..... \tag{4}$$

The effects of $\Delta\boldsymbol{\rho}^{rw}$ and $\Delta\mathbf{h}^{rw}$ on $\Delta\boldsymbol{\rho}_a$ can be expressed and generalized for each ERT electrode configuration by the terms $\Delta\boldsymbol{\rho}_a^{\rho,rw}$ and $\Delta\boldsymbol{\rho}_a^{h,rw}$ as:

$$\Delta\boldsymbol{\rho}_a \approx \mathbf{f}^{\rho} * \Delta\boldsymbol{\rho}^{rw} + a\Delta\mathbf{h}^{rw} + b(\Delta\mathbf{h}^{rw})^2 = \Delta\boldsymbol{\rho}_a^{\rho,rw} + \Delta\boldsymbol{\rho}_a^{h,rw}, \tag{5}$$

where only the $\mathbf{f}^{\rho} * \Delta\boldsymbol{\rho}^{rw} = \Delta\boldsymbol{\rho}_a^{\rho,rw}$ term requires past inputs. We emphasize that each of the 15,500 electrode configurations yields a different $\Delta\boldsymbol{\rho}^a$ time series and therefore needs its own suite of filter coefficients $\mathbf{f}^{\rho}$ and sensitivity factors *a* and *b*.

We estimate the coefficients of the filter function $\mathbf{f}^{\rho}$ and the *a* and *b* terms by deconvolving the output data (apparent resistivity) with the input data (river-water resistivity and river height). This amounts to solving a linear inverse problem for each electrode configuration, in which the filter function $\mathbf{f}^{\rho}$ is regularized by first-order smoothness constraints. For this study, we define the regularization parameter λ_r as the median of parameters estimated from an L-curve analysis (Aster et al., 2005).

Estimation of all parameters requires a period of continuous measurements. For testing the filtering method, we determine $\mathbf{f}^{\rho}$, *a*, *b*, and λ_r for the one-month calibration period 12/06/09 - 01/06/10 (Figs. 2 and 6; Table 2). To obtain the apparent-resistivity time series that we subsequently wish to time-lapse invert, we subtract the contributions caused by variations in the river-water height, $\Delta\boldsymbol{\rho}_a^{h,rw}$ in eq. (5), from the $\Delta\boldsymbol{\rho}_a$ time series. The resulting filtered apparent-resistivity time series $\Delta\boldsymbol{\rho}_a^{f}$, where:

$$\Delta\boldsymbol{\rho}_a^{f} = \Delta\boldsymbol{\rho}_a - \Delta\boldsymbol{\rho}_a^{h,rw}, \quad (6)$$

are expected to be dominated by the time-varying resistivity of the groundwater caused by the infiltrating river water. Application of our method using $\Delta\mathbf{h}^{gw}$ and $(\Delta\mathbf{h}^{gw})^2$ instead of $\Delta\mathbf{h}^{rw}$ and $(\Delta\mathbf{h}^{rw})^2$ in eq. (5) yields practically the same estimates of $\Delta\boldsymbol{\rho}_a^{f}$.

4.2. Stability and predictive capability of the estimated filters

To evaluate the reliability of the filtering method, we first investigate correlations between the temperature-detrended measured $\Delta\boldsymbol{\rho}_a$ values and $\Delta\boldsymbol{\rho}_a$ values simulated using eq. (5). Fig. 6a displays the results for an example electrode configuration for which $\Delta\boldsymbol{\rho}_a$ (median of $\boldsymbol{\rho}_a$ is 147 Ω.m) is clearly affected by $\Delta\mathbf{h}^{gw}$; note how rapid increases in $\Delta\mathbf{h}^{gw}$ (Fig. 6c) cause

strong decreases in apparent resistivity $\Delta\boldsymbol{\rho}^{a}$ (open circles Fig. 6a). The $\mathbf{f}^{\rho}$, *a*, and *b* values used to simulate the $\Delta\boldsymbol{\rho}_{a}$ data shown by solid circles in Fig. 6a are presented in Fig. 6d. The correlation coefficient between the measured and simulated $\Delta\boldsymbol{\rho}_{a}$ time series is 0.98 and the root-mean-square difference is 0.86 Ω.m.

The dashed and dashed-dotted lines in Fig. 6a show the separate contributions of river-water resistivity $\Delta\boldsymbol{\rho}_{a}^{\rho,rw}$ and river-water height $\Delta\boldsymbol{\rho}_{a}^{h,rw}$ to the simulated $\Delta\boldsymbol{\rho}^{a}$ time series. Notice the more pronounced contributions of $\Delta\boldsymbol{\rho}_{a}^{h,rw}$ relative to $\Delta\boldsymbol{\rho}_{a}^{\rho,rw}$ during the significant rainfall-runoff events, the strong anticorrelation of $\Delta\boldsymbol{\rho}_{a}^{h,rw}$ (Fig. 6a) with $\Delta\mathbf{h}^{gw}$ (Fig. 6c), and the strong similarity between $\Delta\boldsymbol{\rho}_{a}^{\rho,rw}$ (Fig. 6a) and $\Delta\boldsymbol{\rho}^{gw}$ measured directly by the loggers in boreholes P3 and P12 (Fig. 6b).

We calculated the mean differences between the measured and simulated $\Delta\boldsymbol{\rho}_{a}$ values for each of the time series during the calibration period. The distribution is centred close to 0 Ω.m (the median in -0.2 Ω.m), with 96% of the configurations having mean absolute differences smaller than 5 Ω.m; this corresponds to a 2.9% error for the relevant apparent-resistivity median value (see Table 2 for these values).

To evaluate the applicability of the filter coefficients defined in Fig. 6d for a different time period, we apply them to the $\Delta\boldsymbol{\rho}^{rw}$ and $\Delta\mathbf{h}^{rw}$ time series recorded during the three weeks starting 5/27/10 and compare the resultant simulated $\Delta\boldsymbol{\rho}^{a}$ time series to the $\Delta\boldsymbol{\rho}^{a}$ time series recorded using the same electrode configuration as in Fig. 6. As shown in Fig. 7, the simulated $\Delta\boldsymbol{\rho}^{a}$ data are a good representation of the measured data; the correlation coefficient between the two time series is 0.92 and the root-mean-square difference is 2.40 Ω.m. Although these values are not as good as for the calibration period, they nonetheless suggest that the system response described by eq. (5) and the estimated parameters are essentially stationary over time.

4.3. Sensitivities

We display the estimated variations of the ERT electrode configurations to changes in Δh^{rw} in Fig. 8. This is achieved by plotting at the centroid positions of the respective 4-electrode configurations the variations in $\Delta\boldsymbol{\rho}_a^{h,\,rw}$ caused by a 1 m rise in river water as predicted by the *a* and *b* factors for each of the electrode configurations. As expected, the most affected configurations are those having electrodes located close to the groundwater table. Sensitivities to water-height variations are less pronounced for configurations with electrodes closer to the river due to the particular style of electrode arrays used. No electrodes are installed in the immediate vicinity (<0.5 m) of the groundwater table in the region close to the river.

4.4. Effectiveness of the filtering method

We now examine the effectiveness of the method in correcting for the unwanted apparent-resistivity component due to $\Delta\mathbf{h}^{gw}$. Fig. 9a shows the distributions of correlation coefficients at zero lag between the two apparent-resistivity series ($\Delta\boldsymbol{\rho}_a$ and $\Delta\boldsymbol{\rho}_a^{f}$) and $\Delta\mathbf{h}^{gw}$ for the calibration period, whereas Fig. 9b shows the distributions of correlation coefficients at zero lag between the two apparent-resistivity series ($\Delta\boldsymbol{\rho}_a$ and $\Delta\boldsymbol{\rho}_a^{f}$) and $\Delta\boldsymbol{\rho}^{gw}$. Apparent resistivities constitute volumetric averaged measurements; different electrode configurations can, for a given phenomena, exhibit sign reversals for the sensitivity coefficients. Therefore, correlations with opposite sign are also possible.

Because there is an approximate 0.5 correlation between $\Delta\mathbf{h}^{rw}$ and $\Delta\boldsymbol{\rho}^{rw}$ (e.g., compare the solid curves in Fig. 2a and b), some degree of correlation is expected between $\Delta\mathbf{h}^{gw}$ and the filtered apparent resistivities $\Delta\boldsymbol{\rho}_a^{f}$. Nevertheless, very few instances of strong negative correlations are found between these latter two time series. For example, whereas 16.7% of the correlation coefficients between $\Delta\mathbf{h}^{gw}$ and $\Delta\boldsymbol{\rho}_a$ lie in the -0.8 to -1 range, only 3.8% of the

coefficients between $\Delta\mathbf{h}^{gw}$ and $\Delta\boldsymbol{\rho}_a^{f}$ have negative amplitudes of comparable magnitude. Particularly noteworthy is the fact that the magnitude of the mean correlation coefficient for $\Delta\mathbf{h}^{rw}$ and $\Delta\boldsymbol{\rho}_a^{f}$ is less than half that for $\Delta\mathbf{h}^{rw}$ and $\Delta\boldsymbol{\rho}_a$ (see legend at the top left of Fig. 9a). There is a noticeable increase in the influence of $\Delta\boldsymbol{\rho}^{gw}$ after water-height filtering (i.e., compare the correlation coefficients between $\Delta\boldsymbol{\rho}^{gw}$ and $\Delta\boldsymbol{\rho}_a$ with those between $\Delta\boldsymbol{\rho}^{gw}$ and $\Delta\boldsymbol{\rho}_a^{f}$ in Fig. 9b) that parallels the decrease in influence of $\Delta\mathbf{h}^{gw}$.

5. Time-lapse inversion of the $\boldsymbol{\rho}_a$ and $\boldsymbol{\rho}_a^{f}$ data sets

We have inverted the 51 $\boldsymbol{\rho}_a^{f}$ data sets acquired during the first 14 days starting 12/07/09 highlighted by the dark gray background in Figs. 2, 3, and 6. Static inversion (Günther et al., 2006; Coscia et al., 2011) of the first of these data sets yielded the reference model. It was recorded under stable hydrogeological conditions. The groundwater height h^{gw} at that time was 392.2 m.a.s.l. and the groundwater resistivity ρ^{gw} varied according to the position of the loggers from 26.9 to 27.8 Ω.m for the 10.7 °C reference temperature. A time-lapse inversion procedure was then applied to the remaining 50 $\boldsymbol{\rho}_a^{f}$ data sets.

5.1 Data selection

Due to the fast dynamics of the aquifer, the apparent resistivities at each electrode configuration vary slightly during the 7-h data acquisition period. In an attempt to avoid temporal smearing of the time-lapse images (Day-Lewis et al., 2003), the smoothly varying apparent-resistivity time series were resampled using spline interpolation to 51 equally spaced time frames, so that the measurements for all electrode configurations each refer to the same times.

All data sets used in the inversions contained measurements for the same selected suite of electrode configurations. A number of criteria were used for the selection. If an estimate of ρ_a^{f}

for any one of the 51 apparent-resistivity time series failed one of the criteria, then all ρ_a^f values for the relevant electrode configuration were eliminated from the time-lapse inversion process. A data point was eliminated if it had:

- any electrode above the groundwater table, since the corresponding data have a near-infinite contact resistance;
- a standard deviation based on repeat measurements > 1%;
- an absolute electrode geometrical factor (Binley and Kemna, 2005) > 1000 to protect against probable low signal-to-noise data;
- anomalously low or high apparent-resistivity values: < 30 Ω.m or > 500 Ω.m.

After the first inversion run to establish the reference model, we also eliminated electrode configurations corresponding to clear outliers for which the apparent resistivities had data misfits > 10 defined as:

$$\frac{\left|\rho_a^f - \rho_a^{model}\right|}{\rho_a^f \cdot \varepsilon}, \tag{8}$$

where ρ_a^{model} is the model-predicted apparent resistivity and ε is the estimated relative error of the data. At this final data selection stage, we had 11,000 ρ_a^f values (corresponding to 71 % of the acquired data) in each of 51 data sets.

5.2. Time-lapse inversion procedure

Time-lapse inversions were performed using the finite-element modelling and inversion code BERT based on the GIMLi library (Günther et al., 2006; Rücker et al., 2006; www.resistivity.net) with models represented by unstructured meshes created using the Tetgen software package (http://tetgen.berlios.de).

We assumed that the surface of the installation field was planar and horizontal at an altitude of 396.26 m.a.s.l., corresponding to the average ground elevation measured at the

eighteen boreholes (maximum difference ±0.25 m), and the riverbank was planar and northward dipping at ~ 40° (Fig. 1c). The topography of the main geological interfaces (i.e., loam - gravel and gravel - clay) was defined by information obtained from drill cores and geophysical logs (neutron-neutron mainly) in each borehole.

The inversion model was defined as a subvolume (~ 67,400 cells) of the forward-model primary mesh (~ 694,000 cells). It was divided into four quasi-layered regions corresponding to the loam, unsaturated gravel, saturated gravel, and clay (Fig. 1c). The interface between the unsaturated and saturated gravel was defined by h^{gw} at background conditions. No model regularization was imposed across regions. The type and degree of regularization λ we employed together with the limits within which resistivities were allowed to vary in each region are defined in Table 3 (see Günther et al. (2006) and Coscia et al. (2011) for further details on our inversion strategy).

After several inversion tests, we decided not to explicitly include the borehole geometries in our time-lapse computations. The borehole fluid effect described by Doetsch et al. (2010a) at the same field site is important for standard 2D electrode configurations, but is only of minor importance for our non-standard circulating 3D ERT configurations (see also Coscia et al., 2011) and is generally less important in time-lapse inversions. In addition, the roughness operator used to regularize the inversion (Günther et al., 2006) does not account for variations in the mesh size. This results in reduced regularization where the mesh elements are small, such that the smoothing constraints are effectively weaker close to the boreholes. Consequently, when including boreholes in the parameterization and using this type of regularization in time-lapse inversions, erroneously strong resistivity variations appear near the boreholes and erroneously small variations are imaged in between the boreholes.

We use a modified version of Daily et al. (1992) to time-lapse invert our data, whereby we invert the logarithms of apparent resistivities recorded at each time step relative to

corresponding apparent resistivities recorded at the beginning of the calibration period and obtain models of electrical resistivity variation with respect to the reference model. In the following, we refer to the time-lapse inversion outputs as the $\delta\rho^{f}$ time-lapse models. We use a noise model ε based on a fixed absolute value of 0.1 mV and a relative error of 1 % . The regularization parameters (initial value λ=30,000 - see Table 3) are successively decreased by a factor of 0.5 at each iteration.

For selecting the final inversion models used in subsequent analyses, we picked for each time frame the models for which either:

- the χ^2 decrease of the data misfit at the subsequent iteration was < 0.1,
- a maximum of 5 iterations.

The final data misfits for the different time-lapse models varied between 0.4% and 2.4%, with a median value of 1.6% (see *Coscia et al.* [2011] for details on how the data are reweighted and errors are redefined during the inversion process). The time-lapse inversions are performed on a 2.66 GHz quad-core computer with 32 GB of RAM.

5.3. Time-lapse inversion of the ρ_a data sub-sets

A useful means to assess the effectiveness of the new filtering method is to compare time-lapse models that result from inverting ρ_a^{f} with (i) time-lapse models that result from inverting ρ_a and (ii) direct measurements of changing groundwater resistivity ρ^{gw}. Accordingly, we have applied the processes described above to the equivalent 50 ρ_a data sets from the 18 boreholes. Because the river-water and groundwater heights at the beginning of the time-lapse inversion period were practically the same as the yearly median values (compare heights in Fig. 2b and Table 2), the reference model for the ρ_a data sets was virtually identical to that for the ρ_a^{f} data sets. Electrode configurations and all inversion parameters chosen for the time-lapse inversion of ρ_a^{f} were also employed for the time-lapse

inversion of ρ_a. We refer to this second suite of time-lapse inversion outputs as the $\delta\rho$ time-lapse models, which again represent resistivity variations relative to the reference model. The final data misfits for the different $\delta\rho$ time-lapse models varied between 1.0% and 3.6%, with a median value of 1.8%.

6. Time-lapse inversion results

In this section, we begin by comparing selected $\delta\rho$, $\delta\rho^{f}$, and $\delta\rho^{gw}$ time series at different locations. To facilitate the comparison, we present all three time series as percent changes relative to the respective values at the start of the inversion period (Fig. 10a - b). To construct $\delta\rho$ and $\delta\rho^{f}$ at a given position, we calculated the mean values within 0.5 m high cylinders of 1 m radius centred at the positions of interest. We then examine vertical slices of the $\delta\rho^{f}$ and $\delta\rho$ models at three selected times (Fig. 11).

6.1 Comparison of resistivity time series

Fig. 10a displays the $\delta\rho^{f}$, $\delta\rho$ and $\delta\rho^{gw}$ resistivity time series at 4.6 m depth in borehole P3 located close to the river (see Fig. 1b). Both $\delta\rho^{f}$ and $\delta\rho$ are correlated with $\delta\rho^{gw}$ and they have similar peak magnitudes, which indicate that both types of inversion explain the main temporal variations of $\delta\rho^{gw}$ at this location. The $\delta\rho^{f}$ curve in Fig. 10a closely mimics the $\delta\rho^{gw}$ curve, thus demonstrating that $\delta\rho^{f}$ is a valid parameter for mapping groundwater resistivity changes associated with infiltrating river water. By comparison, the pattern of $\delta\rho$ variations frequently deviates from that of the $\delta\rho^{gw}$ variations during periods of rapid groundwater-height changes (e.g., isolated outliers at the 1st, 3rd, 9th, 15th data points; shift of the curve at the 20th data point close to the peak resistivity variation). This is attributed to the bias introduced by unaccounted water-height variations, which makes the inversion process less stable.

We anticipate that major changes in the time-lapse models should occur at roughly the same time as the loggers start to sense significant $\delta\rho^{gw}$ variations. This is approximately the case for the $\delta\rho^{f}$ models (compare the crosses in Fig. 10a with the solid curve in Fig. 10b). By comparison, the $\delta\rho$ models contain variations at much earlier times that are unrelated to changes in $\delta\rho^{gw}$ (compare the open circles in Fig. 10a with the solid curve in Fig. 10a), but instead are correlated with changes in δh^{gw} (compare the open circles in Fig. 10a with Fig. 10b). Models obtained by inverting ρ_a^{raw} (i.e., not temperature-detrended) are similar to those obtained by inverting ρ_a, but the peak magnitude is overestimated and the resistivity decrease after the peak value decreases more slowly.

The above observations hold for the majority of $\delta\rho^{f}$ and $\delta\rho$ resistivities reconstructed throughout the aquifer. They highlight the need to account for changing water-level heights before time-lapse inverting the apparent resistivity data.

In the following we investigate how the Δh^{gw} effect shows up throughout the inversion models at specific times.

6.2 Analysis of hydrologically relevant time frames

Figure 10 allowed us to evaluate the performance of our data correction procedure and the inversion results at specific locations. To better evaluate the differences between the $\delta\rho$ and $\delta\rho^{f}$ models, we now examine entire time-lapse inversion models at early times when Δh^{gw} is large. Figure 11 shows vertical slices that have been extracted from the $\delta\rho^{f}$ models (left series of diagrams) and the $\delta\rho$ models (right series of diagrams) at three time steps (see dotted lines in Figure 10):

I. well before any $\delta\rho^{gw}$ variations associated with this event but after the beginning of significant Δh^{gw} variations,

II. immediately after the beginning of $\delta\rho^{gw}$ variations and approximately at the peak of the Δh^{gw} time series,

III. during an initial period of increasing $\delta\rho^{gw}$ (i.e., the first peak) when Δh^{gw} has decreased significantly.

The corresponding data misfits for the $\delta\rho^{f}$ models are 1.4%, 1.5% and 1.4%, whereas the $\delta\rho$ models have data misfits of 1.9%, 2.0% and 2.6%. At time I, the $\delta\rho^{f}$ model (Figure 11a) shows no variations within the aquifer, except for some increases at depth in the middle and in the upper part close to P12, whereas the $\delta\rho$ model (Figure 11b) also shows strong negative changes both in the region close to the groundwater table and close to the clay aquitard. At time II, the $\delta\rho^{f}$ model (Figure 11c) doesn't change appreciably compared to time I, whereas the $\delta\rho$ model (Figure 11d) displays an oscillating behaviour with alternating increasing and decreasing resistivities throughout the aquifer. Times I and II represent times when no appreciable changes are expected in $\delta\rho^{gw}$. We thus find that $\delta\rho^{f}$ display some artefacts, but they appear to be stable with time and localized, while $\delta\rho$ indicate an unstable behaviour with significant inversion artefacts throughout the aquifer volume at times of high Δh^{gw}.

At time III, we expect significant variations in $\delta\rho^{gw}$ throughout the aquifer (see Figure 10a and b), which is in agreement with increases of above 5% in $\delta\rho^{f}$ and $\delta\rho$ in most of the aquifer volume. In the bottom part of the inverted model, $\delta\rho^{f}$ show only minor positive values, while negative values on the order of -5% are seen in $\delta\rho$. All the available $\delta\rho^{gw}$ time series at 8.5 m depth (not shown) indicate only small deviations from zero at this time.

Figures 10 and 11 confirm that our new deconvolution - filtering procedure results in significantly improved imaging of the infiltrating river water into the aquifer at times of significant Δh^{gw} variations. Interpretations based on inverting the uncorrected data would lead

to erroneous arrival-time estimates of the infiltrating river water and other incorrect interpretations.

7. Discussion

Our filtering method for removing unwanted signals could be adapted for other geophysical monitoring situations, provided the main underlying assumptions are satisfied. The most important being that: (1) the input terms can be clearly identified and monitored, (2) the effects of the different signals add linearly, (3) any cross-terms in the input signals can be ignored, (4) the system response is stationary during the time period of interest, and (5) the available time series are longer than the time scales of interest.

The resistivity of the infiltrating river water is higher than that of the groundwater at our study site, but our approach does not depend on the resistivity of the natural source being higher, only different. Essentially the same approach could be used to trace the effects of large volumes of highly polluted low resistivity fluids being accidently released into rivers and their migration into adjacent aquifers. It could also be applied in seawater intrusion investigations and in some artificial tracer experiments. Indeed, fluctuations in the groundwater height may often make it difficult to resolve changes in groundwater resistivity following artificial injection tests, because the injected fluid becomes diluted with time and its salinity is deliberately set at moderate levels in order to decrease density effects. Obviously, our filtering approach would not work at locations where the infiltrating water has the same physical and chemical characteristics as the groundwater.

Although our results suggest that it is possible to remove most of the effects related to groundwater temperature and height, smaller remaining components may continue to affect the data. Unfortunately, it is difficult to account for these remaining components in the inversion process, because they provide bias in the data that cannot be captured in typical

uncorrelated zero-mean noise models. Our approach has therefore been to define a target misfit and the smallest possible regularization weight that provides models that appear largely unaffected by inversion artefacts. This was achieved by gradually decreasing the regularization weight between iterations and by evaluating the resulting inversion models and convergence characteristics at each iteration. The minimum λ was chosen to ensure that all resolved features were larger than roughly half the borehole spacing.

The approach presented here could be improved in different ways, but the main results are likely to be similar. For example, we corrected the raw apparent-resistivity data for seasonal temperature variations, but we neglected the smaller variations (1-2 °C) associated with individual rainfall-runoff events. This latter time-varying effect could be included as a further component in the filtering approach. It would also be preferable to use longer time-periods for estimating the filter function coefficients, but this was not possible due to frequent breakdowns of the data acquisition system. Nevertheless, estimates of filter parameters were similar when our approach was applied to other data acquisition periods.

Because we record a proxy for the natural influence of a massive time-varying line source (the river) and not a punctual or line injection within a borehole, we need to recognize that the spatial resolution of any scheme based on the infiltration of river water will be limited by the distribution of the source.

8. Conclusions

We investigate to what extent ERT apparent resistivity monitoring can be used to investigate groundwater flow patterns by exploiting temporally variable electrical resistivities of infiltrating river water. On the scale of a single rainfall-runoff event, two main phenomena affect variations in temperature-detrended ERT measurements: groundwater-height fluctuations and river water resistivity variations. The first phenomenon determines the

saturated portion of the aquifer and the second controls the time-varying electrical properties of the infiltrating river water, which we wish to use as a natural tracer. Unfortunately, the first phenomenon can completely mask the second during times of large groundwater height variations.

To minimize this problem, we have developed a filtering method that separates the temperature-detrended apparent-resistivity data into contributions due to the different input signals. We have used the method to minimize contributions associated with groundwater-height fluctuations. The resulting filtered ERT data were less correlated with the groundwater height and more correlated with the groundwater resistivity than the unfiltered data.

Three-dimensional time-lapse inversions of the unfiltered and the filtered apparent-resistivity data demonstrate that the inversions of the filtered data result in significantly fewer inversion artefacts. This will make the hydrogeological interpretation of the time-lapse models clearer and helps, for example, to reduce errors related to arrival-time estimations.

In a follow up study, we will use the inversion models together with other relevant geophysical and hydrogeological information to determine 3D flow velocities, flow directions, and arrival times of the infiltrating river water within the groundwater system. It would also be interesting to apply and evaluate (I) the performance of 4D ERT inversions with regularization in time and (II) fully-coupled hydrogeophysical inversion to the filtered data set.

Acknowledgements

We thank our collaborators within the RECORD project, especially Joseph Doetsch and Tobias Vogt, and Christoph Bärlocher for his essential contribution in building and maintaining the ERT monitoring installation. The comments of two anonymous reviewers helped to improve the manuscript. Funding for this study was provided by the Swiss National

Science Foundation (SNF) and ETH's Competence Center for Environment and Sustainability (CCES).

References

Acworth, R.I., Dasey, G.R., 2003. Mapping of the hyporheic zone around a tidal creek using a combination of borehole logging, borehole electrical tomography and cross-creek electrical imaging, New South Wales, Australia. Hydrogeology Journal 11, 368-377. doi: 10.1007/s10040-003-0258-4.

Anderson, M.P., 2005. Heat as a ground water tracer. Ground Water 43, 951-968. doi: 10.1111/j.1745-6584.2005.00052.x.

Aster, R.C., Borchers, B., Thurber, C.H., 2005. Parameter Estimation and Inverse Problems. Academic Press.

Binley, A., Kemna, A., 2005, DC resistivity and induced polarization methods. In: Rubin, Y., Hubbard, S.S. (Eds.), Hydrogeophysics, Springer, 129-156.

Cirpka, O.A., Fienen, M.N., Hofer, M., Hoehn, E., Tessarini, A., Kipfer, R., Kitanidis, P.K., 2007. Analyzing bank filtration by deconvoluting time series of electric conductivity. Ground Water 45, 318-328. doi: 10.1111/j.1745-6584.2006.00293.x.

Cook, P.G., Favreau, G., Dighton, J.C., Tickell, S., 2003. Determining natural groundwater influx to a tropical river using radon, chlorofluorocarbons and ionic environmental tracers. Journal of Hydrology 277, 74-88. doi: 10.1016/S0022-1694(03)00087-8.

Coscia, I., Greenhalgh, S.A., Linde, N., Doetsch, J., Marescot, L., Günther, T., Vogt, T., Green, A.G., 2011. 3D crosshole ERT for aquifer characterization and monitoring of infiltrating river water. Geophysics 76, G49-G59. doi: 10.1190/1.3553003.

Crook, N., Binley, A., Knight, R., Robinson, D.A., Zarnetske, J., Haggerty, R., 2008. Electrical resistivity imaging of the architecture of substream sediments. Water Resources Research 44, W00D13. doi: 10.1029/2008WR006968.

Daily, W., Ramirez, A., LaBrecque, D., Nitao, J., 1992. Electrical resistivity tomography of vadose water movement. Water Resources Research 28, 1429-1442. doi: 10.1029/91WR03087.

Day-Lewis, F.D., Lane, J.W., Jr., Harris, J.M., Gorelick, S.M., 2003. Time-lapse imaging of saline-tracer transport in fractured rock using difference-attenuation radar tomography. Water Resources Research 39, 1290. doi: 10.1029/2002WR001722.

de Franco, R., Biella, G., Tosi, L., Teatini, P., Lozej, A., Chiozzotto, B., Giada, M., Rizzetto, F., Claude, C., Mayer, A., Bassan, V., Gasparetto-Stori, G., 2009. Monitoring the saltwater intrusion by time lapse electrical resistivity tomography: The Chioggia test site (Venice Lagoon, Italy). Journal of Applied Geophysics 69, 117-130. doi: 10.1016/j.jappgeo.2009.08.004.

Diem, S., Vogt, T., Hoehn, E., 2010. Spatial characterization of hydraulic conductivity in alluvial gravel-and-sand aquifers: a comparison of methods. Grundwasser (in German) 15, 241-251. doi: 10.1007/s00767-010-0153-6.

Doetsch, J.A., Coscia, I., Greenhalgh, S., Linde, N., Green, A., Günther, T., 2010a. The borehole-fluid effect in electrical resistivity imaging. Geophysics 75, F107-F114. doi: 10.1190/1.3467824.

Doetsch, J.A., Linde, N., Coscia, I., Greenhalgh, S.A., Green, A.G., 2010b. Zonation for 3D aquifer characterization based on joint inversions of multimethod crosshole geophysical data. Geophysics 75, G53-G64. doi: 10.1190/1.3496476.

Fàlgas, E., Ledo, J., Marcuello, A., Queralt, P., 2009. Monitoring freshwater-seawater interface dynamics with audiomagnetotelluric data. Near Surface Geophysics,7, 391-399.

Günther, T., Rücker, C., Spitzer, K., 2006. Three-dimensional modelling and inversion of dc resistivity data incorporating topography - II. Inversion. Geophysical Journal International 166, 506-517. doi: 10.1111/j.1365-246X.2006.03011.x.

Harvey, J., Wagner, B., 2000. Quantifying hydrologic interactions between streams and their subsurface hyporheic zones. In: Jones, J.B., Mulholland P.J. (Eds.), Streams and Ground Waters. Academic, 3-44. doi:10.1016/B978-012389845-6/50002-8.

Hatch, M., Munday, T., Heinson, G., 2010. A comparative study of in-river geophysical techniques to define variations in riverbed salt load and aid managing river salinization. Geophysics 75, WA135-WA147. doi: 10.1190/1.3475706.

Hayley, K., Bentley, L.R., Gharibi, M., 2009. Time-lapse electrical resistivity monitoring of salt-affected soil and groundwater. Water Resources Research 45, W07425. doi: 10.1029/2008WR007616.

Hayley, K., Bentley, L.R., Gharibi, M., Nightingale, M., 2007. Low temperature dependence of electrical resistivity: Implications for near surface geophysical monitoring. Geophysical Research Letters 34, L18402. doi: 10.1029/2007GL031124.

Hayley, K., Bentley, L.R., Pidlisecky, A., 2010. Compensating for temperature variations in time-lapse electrical resistivity difference imaging. Geophysics 75, Wa51-Wa59. doi: 10.1190/1.3478208.

ISO7888, International Norm, 1985. Water quality - Determination of electrical conductivity. http://www.iso.org/iso/iso_catalogue/.

Kalbus, E., Reinstorf, F., Schirmer, M., 2006. Measuring methods for groundwater - surface water interactions: A review. Hydrology and Earth System Sciences 10, 873-887.

Klotzsche, A., van der Kruk, J., Meles, G.A., Doetsch, J., Maurer, H., Linde, N., 2010. Full-waveform inversion of cross-hole ground-penetrating radar data to characterize a

gravel aquifer close to the Thur River, Switzerland. Near Surface Geophysics 8, 635-649. doi: 10.3997/1873-0604.2010054.

Lesmes, D.P., Friedman, S.P., 2005. Relationships between the electrical and hydrogeological properties of rocks and soils. In: Rubin, Y., Hubbard, S.S. (Eds.), Hydrogeophysics, Springer, 87-128.

Nguyen, F., Kemna, A., Antonsson, A., Engesgaard, P., Kuras, O., Ogilvy, R., Gisbert, J., Jorreto, S., Pulido-Bosch, A., 2009. Characterization of seawater intrusion using 2D electrical imaging. Near Surface Geophysics 7, 377-390.

Nyquist, J.E., Freyer, P.A., Toran, L., 2008. Stream bottom resistivity tomography to map ground water discharge. Ground Water 46, 561-569. doi: 10.1111/j.1745-6584.2008.00432.x.

Ogilvy, R.D., Meldrum, P.I., Kuras, O., Wilkinson, P.B., Chambers, J.E., Sen, M., Pulido-Bosch, A., Gisbert, J., Jorreto, S., Frances, I., Tsourlos, P., 2009. Automated monitoring of coastal aquifers with electrical resistivity tomography. Near Surface Geophysics 7, 367-375.

Olofsson, B., Lundmark, A., 2009. Monitoring the impact of de-icing salt on roadside soils with time-lapse resistivity measurements. Environmental Geology 57, 217-229. doi: 10.1007/s00254-008-1302-4.

Rein, A., Hoffmann, R., Dietrich, P., 2004. Influence of natural time-dependent variations of electrical conductivity on DC resistivity measurements. Journal of Hydrology 285, 215-232. doi: 10.1016/j.jhydrol.2003.08.015.

Rücker, C., Günther, T., Spitzer, K., 2006. Three-dimensional modelling and inversion of dc resistivity data incorporating topography - I. Modelling. Geophysical Journal International 166, 495-505. doi: 10.1111/j.1365-246X.2006.03011.x.

Selker, J.S., Thevenaz, L., Huwald, H., Mallet, A., Luxemburg, W., de Giesen, N.V., Stejskal, M., Zeman, J., Westhoff, M., Parlange, M.B., 2006. Distributed fiber-optic temperature sensing for hydrologic systems. Water Resources Research 42, W12202. doi: 10.1029/2006WR005326.

Slater, L.D., Ntarlagiannis, D., Day-Lewis, F.D., Mwakanyamale, K., Versteeg, R.J., Ward, A., Strickland, C., Johnson, C.D., Lane, J.W., 2010. Use of electrical imaging and distributed temperature sensing methods to characterize surface water-groundwater exchange regulating uranium transport at the Hanford 300 Area, Washington. Water Resources Research 46, W10533. doi: 10.1029/2010WR009110.

Vogt, T., Hoehn, E., Schneider, P., Freund, A., Schirmer, M., Cirpka, O.A., 2010. Fluctuations of electrical conductivity as a natural tracer for bank filtration in a losing stream. Advances in Water Resources 33, 1296-1308. doi: 10.1016/j.advwatres.2010.02.007.

Ward, A., Gooseff, M.N., Singha, K., 2010. Characterizing hyporheic transport processes — Interpretation of electrical geophysical data in coupled stream–hyporheic zone systems during solute tracer studies. Advances in Water Resources 33, 1320-1330. doi: 10.1016/j.advwatres.2010.05.008.

Yeh, T. C. J., Lee, C. H., Hsu, K.C., Illman, W.A., Barrash, W., Cai, X., Daniels, J., Sudicky, E., Wan, L., Li, G.M., Winter, C.L., 2008. A view toward the future of subsurface characterization: CAT scanning groundwater basins. Water Resources Research 44, W03301. doi: 10.1029/2007WR006375.

Table 1. Summary of variables used in the text.

Description	Symbol
River-water height and its variation relative to the yearly median value	h^{rw} and Δh^{rw}
River-water temperature and its variation relative to the yearly median value	T^{rw} and ΔT^{rw}
River-water resistivity and its variation relative to the yearly median value	ρ^{rw} and $\Delta\rho^{rw}$
Groundwater height and its variation relative to the yearly median value	h^{gw} and Δh^{gw}
Groundwater temperature and its variation relative to the yearly median value	$T^{gw}$and ΔT^{gw}
Groundwater resistivity and its variation relative to the yearly median value	ρ^{gw} and $\Delta\rho^{gw}$
Raw apparent resistivity and its variation relative to the yearly median value	ρ_a^{raw} and $\Delta\rho_a^{raw}$
Temperature-detrended apparent resistivity and its variation relative to the yearly median value	ρ_a and $\Delta\rho_a$
Temperature- and groundwater-height-detrended (filtered) apparent resistivity and its variation relative to the yearly median value	ρ_a^{f} and $\Delta\rho_a^{f}$
Simulated change in ρ_a due to changing h^{rw}	$\Delta\rho_a^{h,\,rw}$
Simulated change in ρ_a due to changing ρ^{rw}	$\Delta\rho_a^{\rho,\,rw}$
Model-predicted apparent resistivity	ρ_a^{model}
Variation in groundwater resistivity relative to the value at the beginning of the calibration period	$\delta\rho^{gw}$
Time-lapse resistivities	$\delta\rho$, $\delta\rho^{f}$
Sensitivity factors for apparent resistivity temperature corrections (1 factor per ERT electrode configuration)	k
Filter functions for river-water-resistivity and linear component of river-water-height variations (1 function per ERT configuration)	f^{ρ}, f^{h}
1st and 2nd order filter coefficients for instantaneous response of groundwater-height to river-water-height variations (2 coefficients per ERT electrode configuration)	a, b
Regularization parameter for groundwater-height filter-coefficient estimation	λ_r
Estimated relative error of the data	ε
Regularization parameter for time-lapse inversion	λ

Table 2. For the one-year period (08/20/2009 - 08/20/2010) and the one-month calibration period (12/06/2009 - 01/06/2010), statistics of river-water and groundwater resistivity, height, and temperature together with apparent resistivity. Each apparent resistivity shown in the lower row is determined from the median values calculated for the complete suite of electrode configurations (e.g., the median, maximum, and minimum of the median values for the one-year period are 205.4, 144.1 and 267.0 Ω.m, respectively). Note, that the river-water measurements were made approximately 50 m downstream of the study site.

		Period 08/20/2009-08/20/2010			Period 12/06/2009-01/06/2010		
		Median	Min (Δmin)	Max (Δmax)	Median	Min (Δmin)	Max (Δmax)
River water	Resistivity ρ^{rw} (Ω.m)	32.3	18.1 (-14.2)	65.8 (33.5)	28.2	21.5 (-6.7)	48.1 (19.9)
	Height h^{rw} (m.a.s.l.)	392.1	391.7 (-0.4)	395.0 (2.9)	392.2	391.9 (-0.3)	394.0 (1.7)
	Temperature T^{rw} (°C)	9.0	0 (-9)	26.8 (17.8)	9.3	5.9 (-3.4)	12.4 (3.1)
Groundwater	Resistivity ρ^{gw}(Ω.m)	30.6	22.3 (-8.3)	40.1 (9.5)	28.2	25.6 (-2.6)	30.6 (2.4)
	Height h^{gw}(m.a.s.l.)	392.2	391.9 (-0.3)	393.0 (0.8)	392.2	392.0 (-0.2)	393.0 (0.8)
	Temperature T^{gw}(°C)	10.7	4.2 (-6.5)	20.0(8.7)	6.6	4.8 (-1.8)	8.7 (2.1)
Apparent resitivity ρ_a (Ω.m)		205.4	144.1 (-61.3)	267.0 (61.6)	198.3	170.3 (-28)	214.0 (15.7)

Table 3. Inversion parameters used for each region of the model (see Fig. 1c and Coscia et al. (2011)).

Region	Regularization type	Scaling factor n for the regularization parameter λ	Bounding values ρ_{lower} - ρ_{upper} (Ω.m)
Loam	Damping	10	10-2000
Unsaturated gravel aquifer	Isotropic smoothing	1	50-2000
Saturated gravel aquifer	Isotropic smoothing	1	10-1000
Aquitard (Clay layer)	Damping	10	5-45

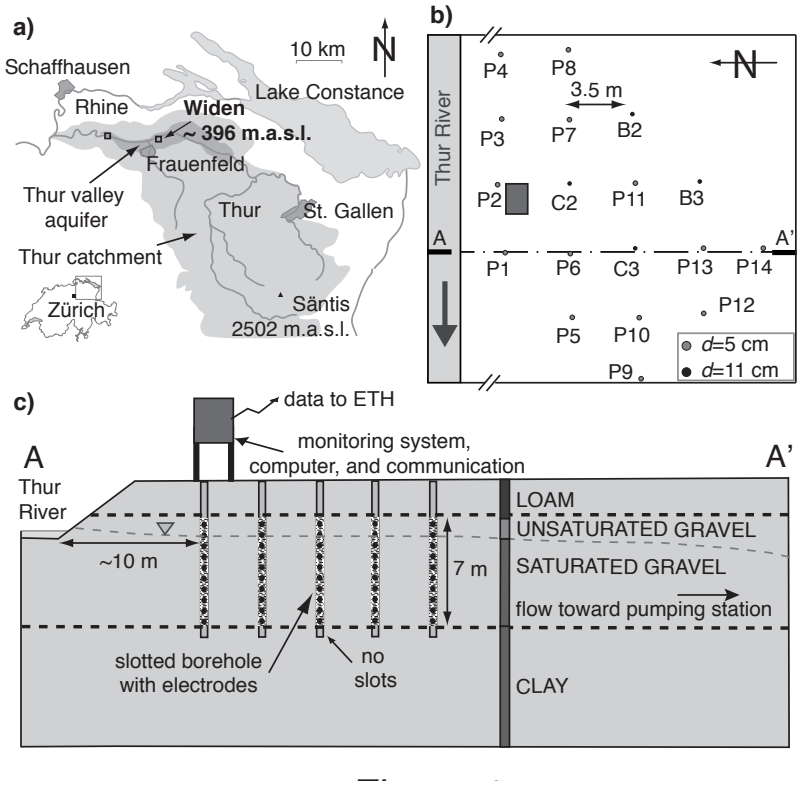

Fig. 1. (a) Location of the Thur River catchment, Thur valley aquifer, and the Widen test site in northeastern Switzerland (modified from a figure prepared by the Swiss Federal Office of Topography). (b) Plan view of part of the Widen site showing borehole positions with respect to the river and flood-proof hut (rectangle between boreholes P2 and C2). Note the orientation of this diagram. (c) Vertical section A'A through the test site (location shown in b) showing electrode installations, stratigraphy, and groundwater level.

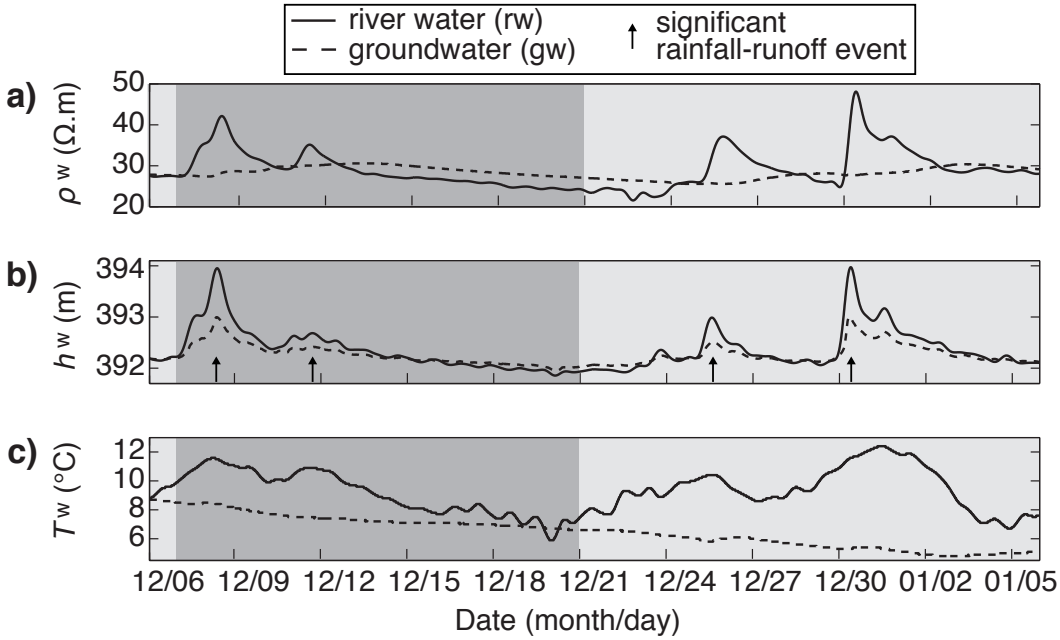

Fig. 2. Variations of river-water and groundwater (a) electrical resistivity, (b) height, and (c) temperature for the one-month calibration period (12/06/09 - 01/06/10). The groundwater data were recorded in borehole P3, approximately 10 m from the river at ~ 6.6 m depth (see Figure 1 for the location). Time-lapse inversions were computed for the 14-day period (12/07/09 - 12/21/09) delineated by the dark gray background.

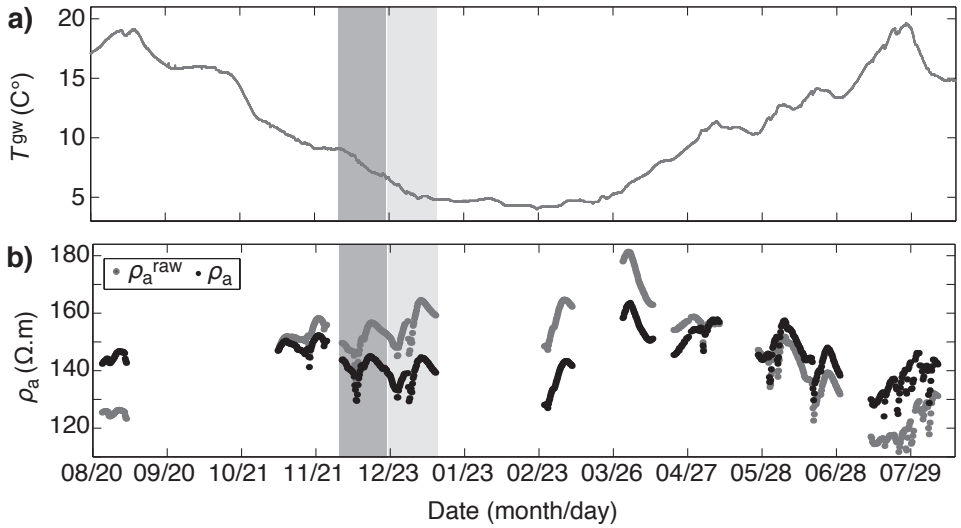

Fig. 3. (a) Groundwater temperatures recorded over a one-year period in 2009-2010. (b) Apparent-resistivity time series for one typical ERT electrode configuration out of a possible 15,500 configurations. Raw ρ_a^{raw} values and temperature-detrended ρ_a values are represented by the closely spaced gray and black dots, respectively. The one-month calibration period (12/06/09 - 01/06/10) is delineated by the two shades of gray background and time-lapse inversions were computed for the 14-day period (12/07/09 - 12/21/09) delineated by the dark gray background.

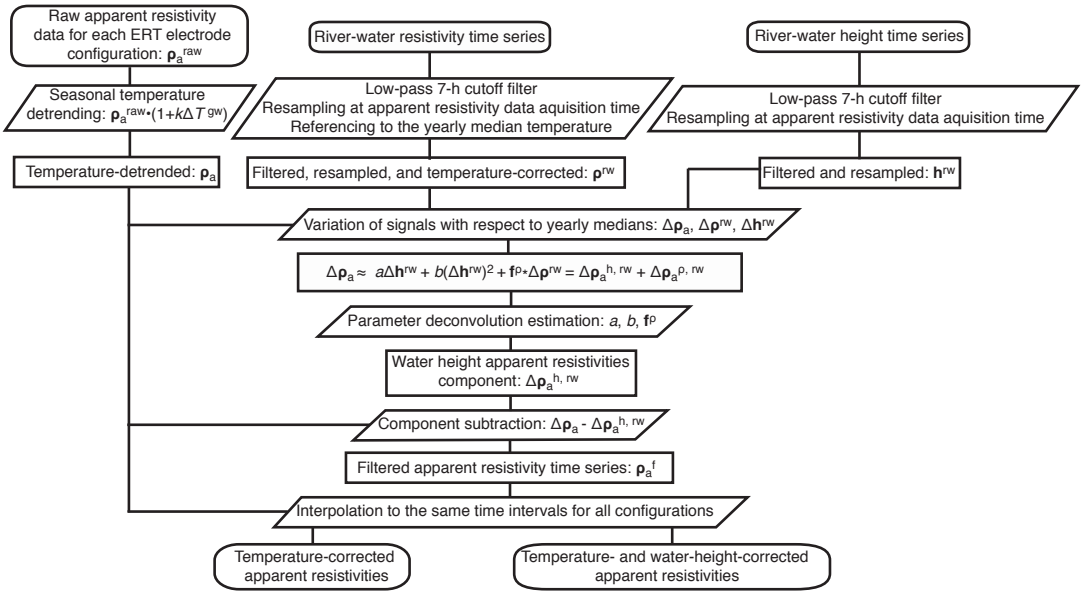

Fig. 4. Summary of processing steps applied to the river-water resistivity and height time series and apparent-resistivity data sets.

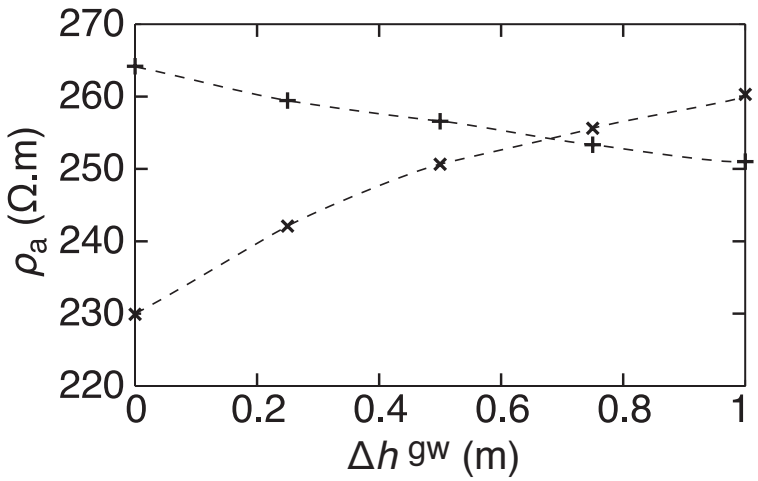

Fig. 5. Results of forward modelling the effects of changing groundwater height on apparent resistivity for two electrode configurations (pluses and crosses; see text for details on the model parameters).

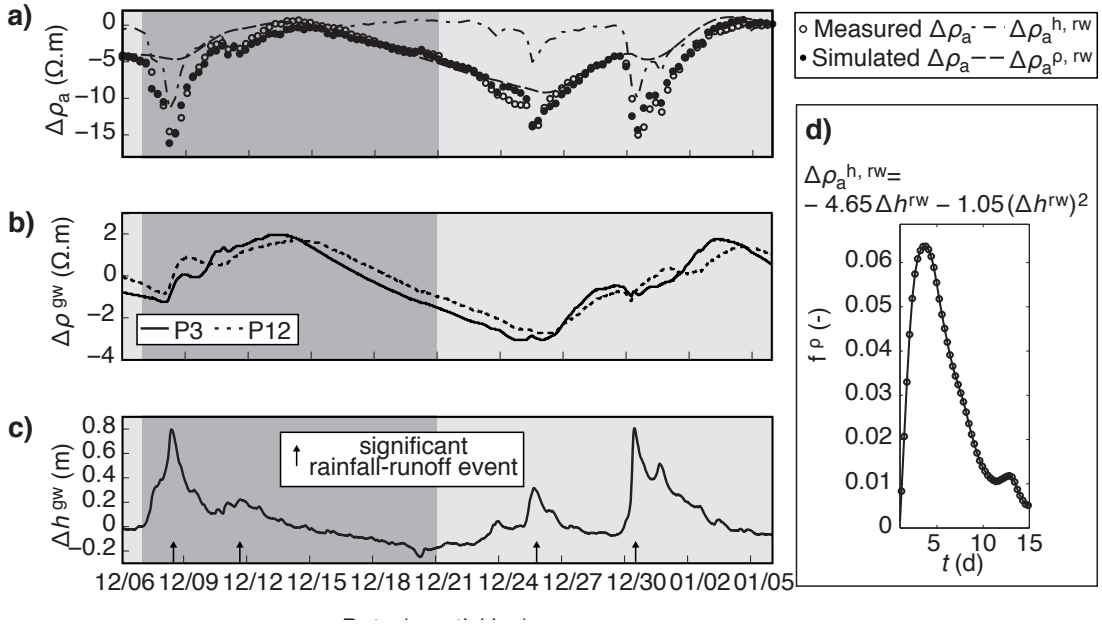

Fig. 6. In all diagrams, the one-month calibration period (12/06/09 - 01/06/10) is delineated by the two shades of gray background and time-lapse inversions were computed for the 14-day period (12/07/09 - 12/21/09) delineated by the dark gray background. (a - c) Variations of $\Delta\boldsymbol{\rho}_a$ (for one example electrode configuration out of the 15,500 measured ones), $\Delta\boldsymbol{\rho}^{gw}$, and $\Delta\mathbf{h}^{gw}$ during the calibration period (values are with respect to the respective yearly median values). (a) Measured $\Delta\boldsymbol{\rho}_a$ (open circles), and simulated $\Delta\boldsymbol{\rho}_a$ (solid circles) as the sum of $\Delta\boldsymbol{\rho}_a{}^{h,\,rw}$ (dashed dotted line; simulated changes in $\Delta\boldsymbol{\rho}_a$ due to changes in river-water height) and $\Delta\boldsymbol{\rho}_a{}^{\rho,\,rw}$ (dashed line; simulated changes in $\Delta\boldsymbol{\rho}_a$ due to changes in river-water resistivity). (b) $\Delta\boldsymbol{\rho}^{gw}$ at two loggers installed in boreholes, one close to the river (continuous line) and the other 15 m further away (dotted line). (c) $\Delta\mathbf{h}^{gw}$. (d) Quadratic equation represents $\Delta\boldsymbol{\rho}_a{}^{h,\,rw}$ in terms of the $\Delta\mathbf{h}^{rw}$ time series, whereas the graph shows the filter function $\mathbf{f}^{\rho}$ that is convolved with the $\Delta\boldsymbol{\rho}^{rw}$ time series to give $\Delta\boldsymbol{\rho}_a{}^{\rho,\,rw}$ (see Figure 4 and text)

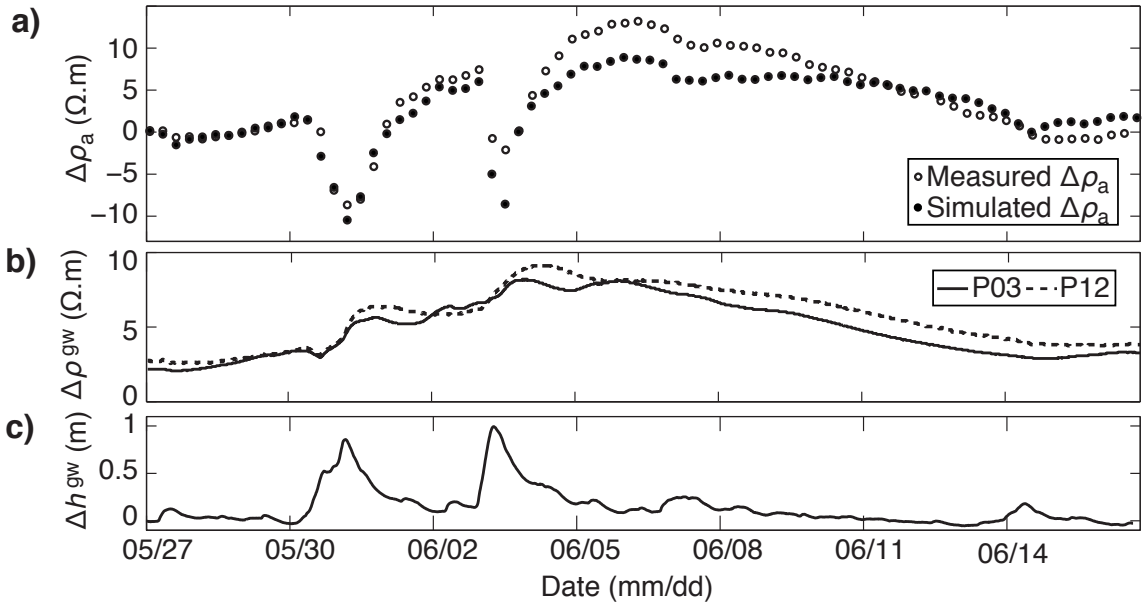

Fig. 7: (a) Comparison between the measured (open circles) and simulated (solid circles) $\boldsymbol{\rho}_a$ time series for a period outside of that used for the calibration. (b) $\Delta\boldsymbol{\rho}^{gw}$ at two point loggers, one close to the river (continuous line) and the other 15 m further away (dotted line). (c) $\Delta\mathbf{h}^{gw}$. Values in all diagrams are relative to the respective yearly median values.

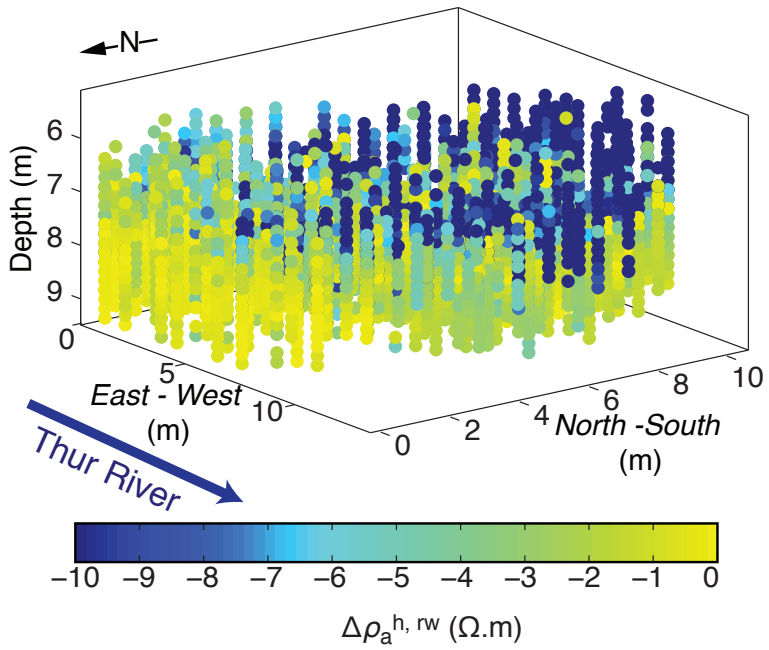

Fig. 8: (a) Variations of apparent resistivities $\Delta\rho_a^{h,\,rw}$ due to a 1 m increase in h^{rw}. The data are plotted at the centroid positions of the respective electrode configurations. Note that the scale is clipped at 0 to emphasize the negative sensitivities (see Fig. 9).

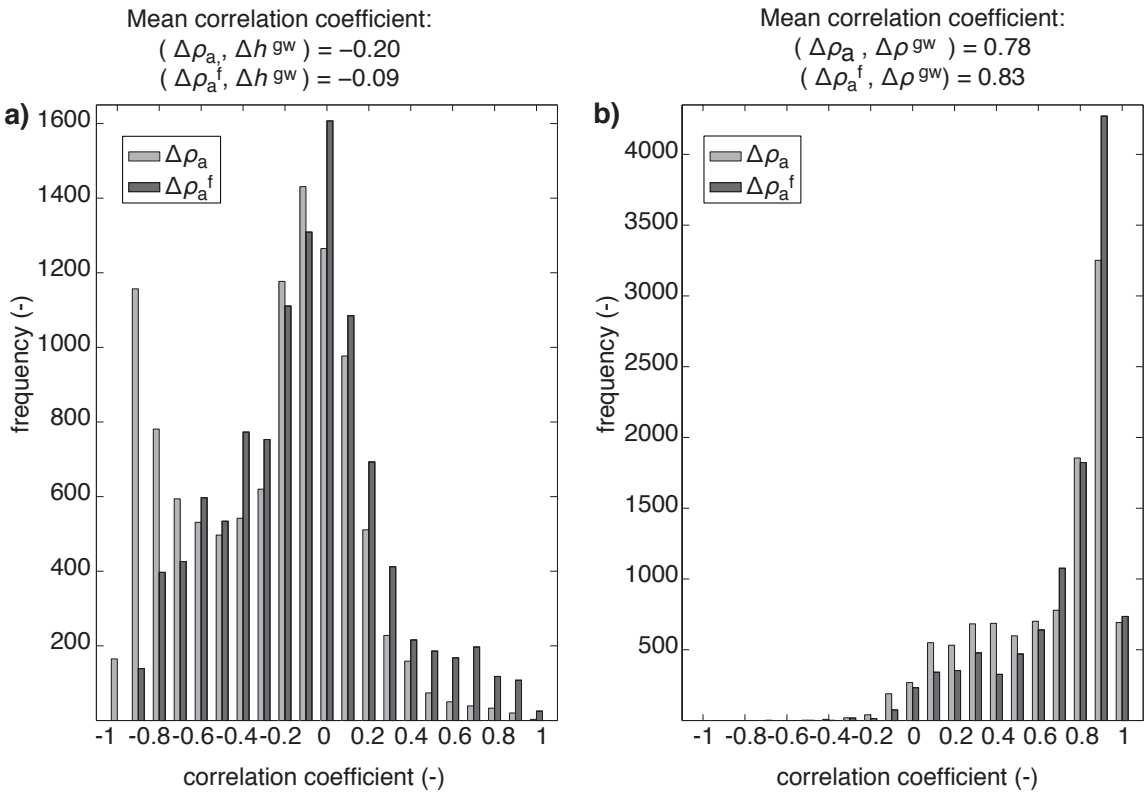

Fig. 9: For the calibration period and for all ERT electrode configurations, distribution of correlation coefficients between the raw and filtered apparent resistivities $\Delta\boldsymbol{\rho}_a$ and $\Delta\boldsymbol{\rho}_a^f$ and (a) $\Delta\mathbf{h}^{gw}$ and (b) $\Delta\boldsymbol{\rho}^{gw}$.

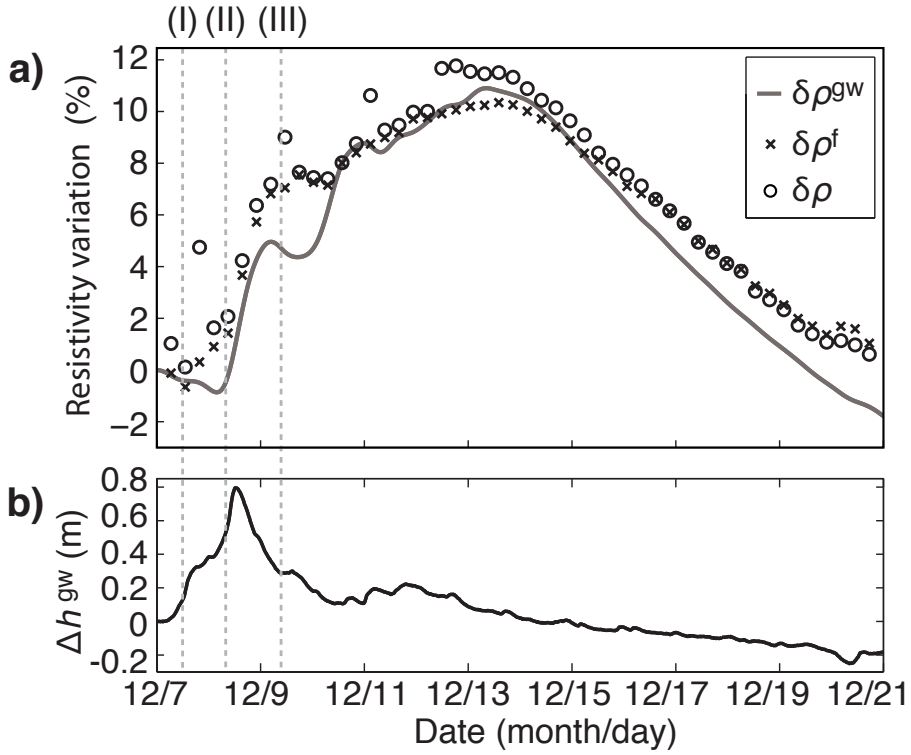

Figure 10. (a) Time series of resistivities extracted from the $\delta\rho$ (open circles) and $\delta\rho^{f}$ (solid circles) time-lapse models at 4.6 m depth in P3 together with percent changes in groundwater resistivity $\delta\boldsymbol{\rho}^{gw}$ relative to the respective values at the beginning of the calibration period. Dashed vertical lines identify times I - III for which vertical slices are shown in Figure 11. (b) $\Delta\mathbf{h}^{gw}$.

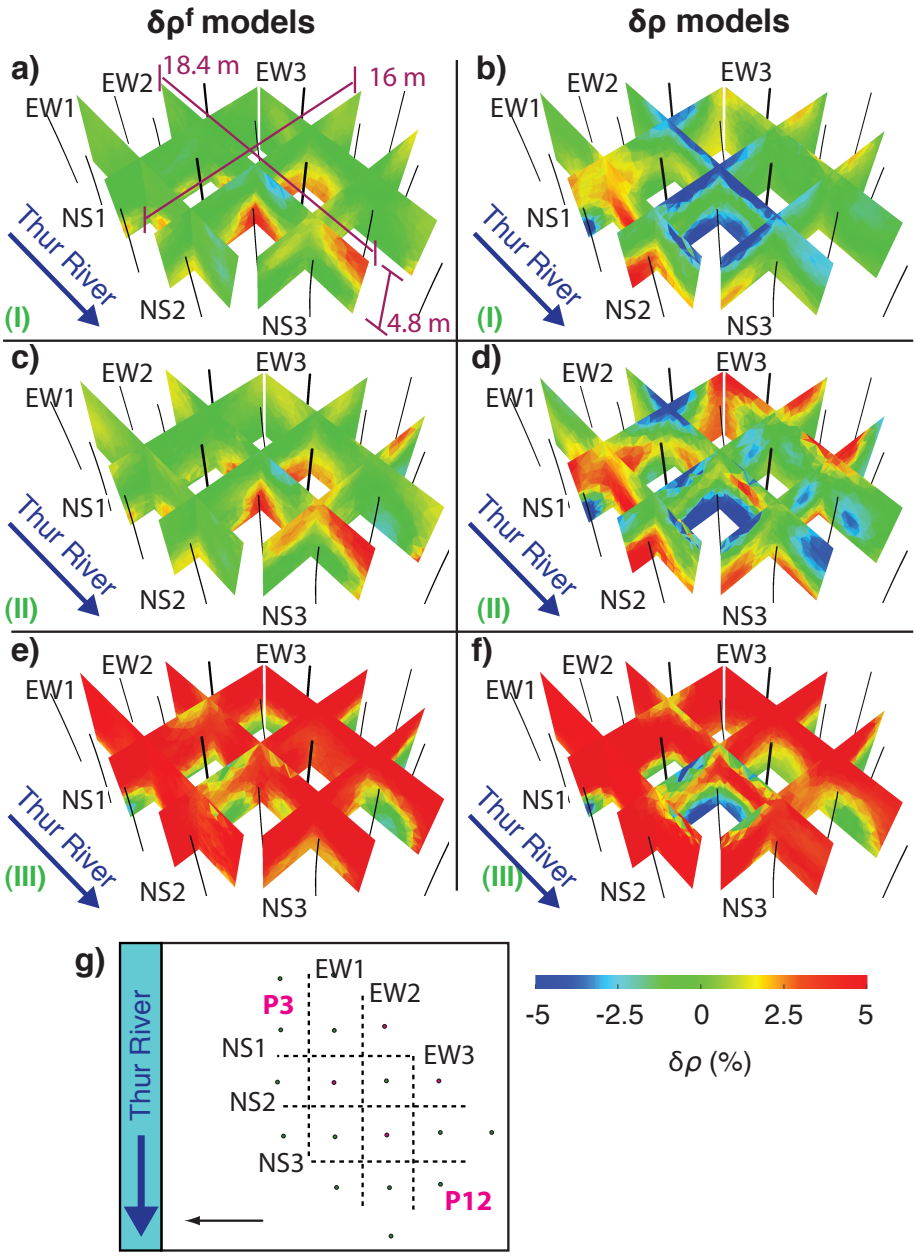

Figure 11. Vertical slices of resistivity variations extracted from the δρ and $\delta\rho^f$ time-lapse models at times I – III shown in Figure 10a - c: (a) and (b) time (I), (c) and (d) time (II), (e) and (f) time (III). Diagram (g) indicates the position of the slices with respect to the river. Left and right columns of diagrams are for the δρ and $\delta\rho^f$ time-lapse models. Note that only the aquifer region is shown, but that the properties of the surrounding regions (top soil, unsaturated zone, clay aquitard) were also inverted for (c.f., Figure 6 in Coscia et al. (2011)).